

Contents lists available at ScienceDirect

Acta Materialia

journal homepage: www.elsevier.com/locate/actamat



Athermal resistance to phase interface motion due to precipitates: A phase field study



Mahdi Javanbakht^{a,*}, Valery I. Levitas^{b,c}

- ^a Department of Mechanical Engineering, Isfahan University of Technology, Isfahan 84156-83111, Iran
- ^b Department of Mechanical Engineering, Iowa State University, Ames, IA 50011 USA
- ^c Department of Aerospace Engineering, Iowa State University, Ames, IA 50011 USA

ARTICLE INFO

Article history: Received 8 June 2022 Revised 19 October 2022 Accepted 27 October 2022 Available online 29 October 2022

Keywords: Precipitate Critical thermal driving force Hysteresis Phase field theory High pressure phase

ABSTRACT

Athermal resistance to the motion of a phase interface due to a precipitate is investigated. The coupled phase field and elasticity equations are solved for the phase transformation (PT). The volumetric misfit strain within the precipitate is included using the error and rectangular functions. Due to the presence of precipitates, the critical thermal driving forces (athermal friction) remarkably differ between the direct and reverse PTs, resulting in a hysteresis behavior. For many cases, the critical thermal driving force increases like c^x , x=0.5-0.6, vs. the precipitate concentration c for both the direct and reverse PTs. This is similar to c^{0.5} for the known effect of solute atoms on the athermal friction, which are also dilation centers, but without surface energy. Change (40% reduction) in the precipitate surface energy during PT significantly changes the PT morphology and the critical thermal driving forces. For the precipitate radius small compared to the interface width, the misfit strain does not practically show any effect on the critical thermal driving force. In the opposite case, for both the constant surface energy (CSE) and variable surface energy (VSE) boundary conditions (BCs) at the precipitate surface, the critical thermal driving force linearly increases vs. the misfit strain for the direct PT while it is almost independent of it for the reverse PT. For any concentration, the VSE BCs result in higher thermal critical driving forces, but a smaller hysteresis range, and a larger transformation rate. The obtained critical microstructure and thermal driving forces are validated using the thermodynamic phase equilibrium condition for stationary interfaces. Increase in the interface width reduces the interphase friction. After neglecting misfit and transformation strain and change in surface energy, our simulations describe well the Zener pinning pressure for the grain boundary. The obtained results give an important generic understanding of athermal friction mechanism for phase interfaces for various PTs at the nanoscale.

© 2022 Acta Materialia Inc. Published by Elsevier Ltd. All rights reserved.

1. Introduction

Phase interface friction and athermal hysteresis. The interaction of PTs with structural defects plays a crucial role in determining transformational properties of materials. Athermal interface friction which significantly affects the thermodynamics, kinetics, and morphology of martensitic PTs can be caused by the Peierls barrier, interaction of the interfaces with grain and subgrain boundaries and stacking faults, dislocations, point defects [1–3], and precipitates, which were not included in the above treatments. Here, we will focus on the interaction of the phase interface and precipitates (or inclusion of other materials or phases, which for our general treatment do not differ from the precipitates), which was not suffi-

ciently studied theoretically. The experimental study of martensitic PT in a β -CuAlBe shape-memory alloy in [4] revealed a significant change in morphology and thermodynamic PT conditions due to precipitates. Experiments in [5] found significant influence of the defects such as precipitates on austenite-martensite interfaces on the thermoelastic PT equilibrium in CuAlNi. Based on experiments, an internal friction model was suggested based on the theory of phase nucleation and growth at the microscale which shows the significant change in the thermoelastic martensitic transformation due to interstitials [6]. The significant effect of Ni₄Ti₃ nanoprecipitates on the stress- and temperature-induced PTs, superelastic hysteresis loop, transformation temperatures and other characteristics of NiTi under uniaxial compression was found using MD simulations in [7,8]. A larger hysteresis occurred for the model with precipitates compared to the pristine NiTi due to the hindrance of reverse PT. In contrast, precipitates in NiTi elastocaloric materials are used to reduce PT hysteresis and energy loses [9,10]. This

^{*} Corresponding author.

E-mail address: javanbakht@iut.ac.ir (M. Javanbakht).

was rationalized in terms of precipitate-induced martensite nucleation. This process was studied using phase field approach (PFA) in [11] which deals with the effect of the matrix-precipitate interface energy and width on the martensite nucleation rather than with the athermal friction to the interface propagation.

Usually, kinetic equations for thermally activated interface motion are derived by considering some spatially oscillating energy profile that mimics the Peierls barrier and the energy profiles of various defects [1,2]. In the PFA, an oscillating in space energy profile is introduced through oscillating stress fields of some defects or through the oscillating contribution the jump in chemical energy [12,13], which resulted in the athermal interface friction and PT hysteresis. The athermal hysteresis was also obtained within the PFA due to the dislocations generated along the austenitemartensite interface [14]. Such hysteresis behavior is even more crucial for PTs from the low-pressure phases (LPP) to high-pressure phases (HPPs), which occur with a broad range of transformation pressures. Many HPPs (e.g., diamond and cubic BN) have various desired physical properties, in particular, very large hardness. One of the goals in the synthesis of HPPs is to reduce PT pressure for direct PT and to suppress the reverse PT, so that HPPs can be used at normal pressure in engineering applications. That is why controlling athermal interface friction, in particular by precipitates and inclusions can play a key role on the LPP-HPP transformation characteristics in various materials. Recent reviews that include analysis of hysteretic behavior for HP PTs are presented in [15-17]. Despite the extensive research on HPPs, the athermal friction to the phase interface motion and the hysteresis in HPPs due to precipitates have not been studied yet, and this is the main focus of the current work. Within linear elasticity and small strain formulation, the effect of external uniform pressure (stresses) produces additive contribution to the total stresses. Since our focus is to find the athermal interface resistance due to internal and interfacial stresses and change in the surface energy, we will not apply external load, but thermal hysteresis can be recalculated into pressure hysteresis using known equations.

Effect of precipitates on the grain boundary motion. There exist various analytical, numerical, and experimental works on the effect of particles and precipitates on the grain boundary (GB) motion. 3D FEM simulations for GB motion through spherical incoherent particles were presented based on a variational formulation for boundary motion by viscous drag [18], where the drag force deviates from the Zener drag theory due to the high density of particles on the GB. An experimentally proven model for predicting austenite grain growth including the pinning and solute-drag effects of TiNi precipitates and assuming a constant width of an austenite grain boundary was proposed in [19]. The effect of the interfacial energy of grain/particle was studied on grain growth kinetics using a cellular automata model [20], where the particles showed both the Zener pinning and non-Zener pinning effects. The key role of temperature and composition on the interaction between Ta clusters and GBs was revealed in [21]. A random walk model for GB motion through particles was introduced [22] which attributes GB fluctuations to the boundary mobility and drag effect. Effective parameters on pinning of a Cu GB by an Ag particle were studied using molecular dynamics simulations [23,24]. Experiments revealed both the solute drag and precipitate Zener effects are responsible for recrystallization in Zr-Nb alloys [25]. The kinetics of austenite grain growth was predicted in agreement with experiments using both the precipitation and grain growth models [26]. The effect of particles and precipitates on the interfaces is also investigated in few works. A significant Zener effect was found during annealing in Al-Mg-Si alloy due to the high density of the L12 dispersoids [27]. The interaction between interfaces and precipitated carbides was experimentally studied in [28], in which the shifts in the critical temperatures were attributed to the pinning force in agreement with the classical Zener theory. In the current paper, we will show that when we neglect all differences between phase interface and GB, we can reproduce within our PFA an analytical result for the Zener pinning pressure. Zener pinning is more than order of magnitude smaller than what we obtain for the interaction between a precipitate and phase interface.

PFA was applied to simulations of interaction of GBs and pinning inclusions [29-32]. 3D PF simulations of moving GBs through cylindrical particles in composites were presented and the effect of relative orientation and aspect ratio of particles on the kinetics was studied [29]. 3D PF simulations for the grain growth were performed which revealed the effect of particle-matrix coherency (but without introducing stresses) on GB pinning [30]. A PFA was proposed to study the effect of coherent precipitate on the Zener pinning of GBs which includes the misfit strain and the elastic heterogeneity and anisotropy [31]. The PF simulations were performed for 2D and 3D polycrystalline materials, and the pinning effect of incoherent particles (also without stresses) on GBs was studied [32]. The main result is that increase in misfit strain, elastic inhomogeneity and anisotropy mostly reduce the Zener pinning through coherent precipitate. However, this paper studied collective effect of multiple particles and GBs, while we are interested in the interaction between individual precipitate and phase inter-

To summarize, we are not aware of any study of the interaction of a precipitate/inclusion with phase interface which considers relevant mechanics, and this is the focus of the current work. In the current paper, we present the first detailed PFA study of the athermal friction to the interface motion caused by a precipitate, which includes (a) two different profiles of a mismatch strain within an interface, (b) unchanged and varied precipitate surface energy during the PT, (c) transformation strain with volumetric and shear components (for cubic to hexagonal lattices) and the analysis of their effects, as well as the effect of the precipitate size, phase interface width, and volume fraction of the precipitates. The paper is organized as follows. In Section 2, the phase field model as well as the precipitate model are presented. We implement advanced PFA developed in [33-35] which satisfies formulated conditions and reproduces the desired stress-strain curves, PT conditions under action of the stress tensor, and known properties of each phase in thermodynamic equilibrium under stresses, in contrast to all other models. This model is supplemented by surface-induced PTs and interface stresses presented in [36-39], which was used for precipitates only in our paper [11] but for nucleation at the precipitate rather to determine athermal friction. The numerical procedure is described in Section 3. The results including critical thermal driving forces vs. precipitate concentration and misfit strain for direct and reverse PTs and corresponding nanostructures, hysteresis region, nanostructure evolution during direct and reverse PTs, size effect, interface width effect and the effect of precipitate variable surface energy on the critical driving forces are presented with their discussion in Section 4. Correspondence of our result after all required simplifications with the Zener theory is proved. Concluding remarks are summarized in Section 5.

2. System of equations

Since this is the first detailed phase-field study of the effect of interaction of the precipitate and phase interface, we want to find some generic results. That is why we choose the same isotropic material and surface energy models and some reasonable material parameters from phase-field papers [40,41], where the same first-order transformation between the cubic LPP to the hexagonal HPP is studied without precipitate, and then we vary some material parameters. The pinning precipitate is also specified in a generic term, like coherent inclusion with misfit strain without direct

Table 1The material parameters used in the PT simulations.

Parameter	Value	Definition
A_0	20.6 MPaK ⁻¹	The magnitude of the double well
		barrier between LPP-HPP
Z	-5.05 MPaK^{-1}	The jump in specific entropy
β	$5.18 \times 10^{-10} \text{ N}$	LPP-HPP gradient energy coefficient
λ	2600 (Pa.s) ⁻¹	Kinetic coefficient
θ_{e}	100 K	Phase equilibrium temperature at zero
		stress
$\theta_{ m c}$	−90 K	Critical temperature for the loss of
		stability of the stress-free LPP
E	177.023 GPa	Young's modulus
ν	0.238	Poisson's ratio
$arepsilon_{tr}$	$\begin{bmatrix}05 & 0.1 \\ 0.1 &05 \end{bmatrix}$	Transformation strain tensor

relation to the transforming phases, with a generic circular shape; that is why its size can be varied independently. The surface energy of the inclusion varies (reduces by 40%) during the PT. While this model supplemented by PFA for dislocation evolution was applied to describe various aspects of interaction between PT and dislocations [14,42], here we neglect dislocation nucleation and evolution to understand behavior of elastic material first. Dislocations will be added in a future work.

2.1. Phase field model for LPP-HPP transformation [18,20]

An order parameter, η , varies from 0 for the parent phase (which we will call LPP, while it is equally applied to temperature-induced PT) to 1 for HPP. The transformation between the LPP and the HPP is described using the Ginzburg-Landau (GL) equation for the evolution of the order parameter η as

$$\frac{1}{\lambda} \frac{\partial \eta}{\partial t} = -\frac{\partial \psi_P}{\partial \eta} |_{\varepsilon} + \beta \nabla^2 \eta. \tag{1}$$

The Helmholtz free energy per unit volume ψ_P is defined as

$$\psi_{P} = \frac{1}{2} \varepsilon_{e} : C : \varepsilon_{e} + A_{0}(\theta - \theta_{c}) \eta^{2} (1 - \eta)^{2}$$

$$+ z(\theta - \theta_{e}) \eta^{3} (4 - 3\eta) + \frac{\beta}{2} |\nabla \eta|^{2}.$$

$$(2)$$

Here, θ is the temperature, $\theta_{\rm e}$ is the phase equilibrium temperature at zero stresses, $\theta_{\rm c}$ is the critical temperature for the loss of stability of the stress-free LPP, $\varepsilon_{\rm e}$ is the elastic strain tensor, and C is the tensor of elastic moduli. The material parameters λ , β , z, and A_0 are defined in Table. 1. For these parameters, the interface width $\delta_0 = 5.54 \sqrt{\beta/(2A_0(\theta_{\rm e}-\theta_{\rm c}))} = 1.43$ nm and energy $\gamma = \sqrt{\beta A_0(\theta_{\rm e}-\theta_{\rm c})/18} = 0.36$ J/m². The transformation strain tensor ε_t varies from zero for LPP to ε_{tr} for HPP as

$$\boldsymbol{\varepsilon_t} = \boldsymbol{\varepsilon_{tr}} \left[a\eta^2 + (4 - 2a)\eta^3 + (a - 3)\eta^4 \right], \tag{3}$$

where a is a material parameter which characterizes the PT equilibrium and instability pressures [33] and will be determined below. For the total strain tensor $\boldsymbol{\varepsilon}$ we accept the additive decomposition of elastic ($\boldsymbol{\varepsilon}_{\rm e}$), transformation ($\boldsymbol{\varepsilon}_{\rm t}$), and precipitate misfit ($\boldsymbol{\varepsilon}_{pr}$) strain tensors as

$$\boldsymbol{\varepsilon} = \boldsymbol{\varepsilon}_{e} + \boldsymbol{\varepsilon}_{t} + \boldsymbol{\varepsilon}_{pr}. \tag{4}$$

For convenience of describing the material in terms of characteristic pressures instead of temperatures, we introduce the phase equilibrium pressure, $p_{\rm e}$, and the lattice instability pressures for the direct PT, $p_{\rm in}$, and reverse PT, $p_{in}^{\rm r}$, as [33,34,40,43]

$$p_{\rm e} = \frac{z(\theta - \theta_{\rm e})}{\varepsilon_{\rm 0}}$$

$$p_{\text{in}} = \frac{A_0(\theta - \theta_{\text{c}})}{a\varepsilon_0}$$

$$p_{\text{in}}^r = \frac{6z(\theta - \theta_{\text{e}}) - A_0(\theta - \theta_{\text{c}})}{(6 - a)\varepsilon_0}.$$
(5)

We accept $p_e=10$, $p_{\rm in}=20$, and $p_{in}^r=-10$ at $\theta=300K$ [40]. For the plain-strain formulation, the volumetric transformation strain $\varepsilon_0=(\varepsilon_{trx}+\varepsilon_{try})=-0.1$, see Table 1. Substituting these values in Eq. (5) gives a=4, $A_0=20.6MPa$, and $z=5.05MPaK^{-1}$. The elasticity equations which will be coupled to the GL equation are

$$\nabla \cdot \sigma = 0$$

$$\varepsilon = \varepsilon_{e} + \varepsilon_{tr} + \varepsilon_{pr} = \frac{1}{2} \left[\nabla u + (\nabla u)^{T} \right]$$

$$\sigma = C : (\varepsilon - \varepsilon_{tr} - \varepsilon_{pr}), \tag{6}$$

where σ is the elastic stress tensor and u is the displacement field. Substituting Eqs. (3) and (6) with a=4 into Eq. (1) gives the GL equation as

$$\frac{1}{\lambda} \frac{\partial \eta}{\partial t} = 4\eta (\eta - 1)(\eta - 2)\sigma :$$

$$\varepsilon_{tr} - \left[2A_0(\theta - \theta_c) \ \eta(\eta - 1)(2\eta - 1) + 12z(\theta - \theta_e)\eta^2(1 - \eta) \right]$$

$$+ \beta \nabla^2 \eta$$
(7)

The insulated boundary condition for the PT problem is $\beta \nabla \eta. n = 0$, where n is the normal to the boundary. It means that the surface energy of the external boundaries does not change during the PT.

2.2. Precipitate model

The precipitate is modeled as a non-evolving circular region inside which no PT occurs and it includes a misfit strain due to the compositional heterogeneity between the matrix and precipitate [31,44]. The corresponding misfit strain tensor with respect to LPP is modeled as a position dependent volumetric strain $\varepsilon_{pr} = \varepsilon_{p}(x)I$ [31], where x is the position vector and I is the unit tensor. The position dependence or the distribution of $\varepsilon_p(x)$ is considered using two different models: (a) a jump function such that $\varepsilon_p(x) = \varepsilon_V$ inside the precipitate region and it is zero in the rest of sample, where $\varepsilon_{\rm v}$ is the misfit strain coefficient, and (b) the error function $\varepsilon_{\rm p}({\bf x}) = \varepsilon_{\rm v}/(\pi l^2) \exp(-|{\bf x}'-{\bf x}|^2/l^2)$, where l is the radius of the circular region with the center x', within which $\varepsilon_p(x)$ is nonzero [45] and smoothly goes to zero outside of it. Our results show practically no difference between these two models due to the nanoscale size of the precipitate. The precipitate concentration, c, is defined as the ratio of the area of the precipitate to that of the entire sample. The misfit strain is assumed to be independent of the order parameter. Here, a range of compositional heterogeneity due to different types of precipitate is characterized by the range $0 \le \varepsilon_{\rm V} \le 0.1$ for the misfit strain. In practice, due to its additivity with volumetric part of the transformation strain, this means that the misfit constant with respect to the HPP is $\varepsilon_{\rm v} + 0.5\varepsilon_{\rm 0}$. Since misfit strain is considered to be tensile, it produces internal compressive mean stress (pressure) in the precipitate and tensile mean stress in the matrix. These stresses suppress direct and promote reverse PTs. Note that the study of the effect of misfit strain on grain growth and GB motion was presented in [31,44], where it was considered independent of GBs.

The boundary between the precipitate and matrix is coherent, i.e., displacements are continuous across the interface. The surface energy of the precipitate during the PT can vary or be constant. The variable surface energy boundary conditions (VSE BCs)

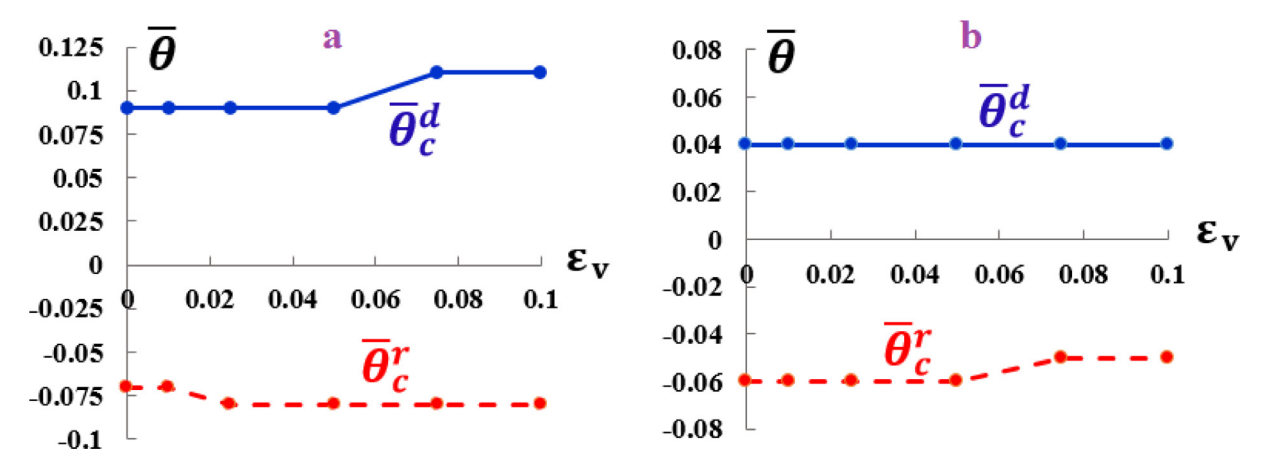


Fig. 1. The critical thermal driving forces for direct (blue lines) and reverse PTs (red lines) vs. the misfit strain coefficient for (a) the misfit strain distribution using the error function and (b) for the constant misfit strain; L=20 and R=0.5, i.e., c = 0.002. There is clear effect of the shape of ε_v .

between the precipitate and the matrix [11,36,37] are defined as

$$\beta \nabla \eta.n = -\frac{d\gamma}{d\eta},$$

$$\gamma = \gamma_{LPP} + (\gamma_{HPP} - \gamma_{LPP}) [a\eta^2 + (4 - 2a)\eta^3 + (a - 3)\eta^4],$$
(8)

where γ is the variable surface energy between inclusion and matrix during the PT, and γ_{LPP} and γ_{HPP} are the surface energies between the precipitate and the LPP and HPP, respectively. For the constant surface energy (CSE) BCs, $\gamma_{HPP} = \gamma_{LPP}$ and $\beta \nabla \eta.n = 0$. Since $\nabla \eta$ describes the normal to the LPP-HPP interface, then this interface is orthogonal to the precipitate surface. We accept for VSE BCs that $\gamma_{LPP} = 1 \ J/m^3$ and $\gamma_{HPP} = 0.6 \ J/m^3$. The reduction in surface energy promotes HPP and suppresses LPP.

3. Numerical procedure

The FEM COMSOL code is used to solve the coupled GL and elasticity equations in 2D, which are implemented in PDE/Heat Transfer in Solids application and the Structural mechanics/Plane Strain application, respectively. Triangle Lagrange elements with quadratic approximation for the displacements and order parameter are used. Hence, total strain is interpolated linearly and transformation and, consequently, elastic strains are interpolated nonlinearly. This does not cause any issue with the stress results when at least 5 quadratic triangular Lagrangian elements are used along the interface thickness [39]. The maximum mesh size of 0.25 nm are used; i.e., it means at least 5 elements are used along the interface thickness to reach mesh-independent solutions. Due to the circular domain embedded inside a square, the mesh pattern is heterogeneous. The mesh size can be automatically chosen smaller in certain parts due to the automatic refinement depending on the precipitate size. Even for the precipitate with R=0.5 there are more than 8 elements along its diameter. The Segregated solver with the time step of 0.01ps has been utilized. Stress, size, and time are normalized by 1 GPa, 1 nm, and 1 ps, respectively. The material parameters for the PT simulations [40,41] are given in Table 1. Note that negative critical temperature for the loss of stability of the stress-free LPP does not contradicts the third law of thermodynamics. Indeed, based on the definition of the barrier energy coefficient between the LPP and HPP, $A = A_0 (\theta - \theta_c)$ [33]; since Ais positive at zero temperature, the extrapolation of A to its zero value gives negative temperature θ_c . This means that the LPP is stable or metastable for any temperature down to OK, and application of stresses can cause the PT only. The numerical solutions well resolve the analytical solutions for the planar austenite-martensite interface energy and width [40-42].

4. Results

The athermal resistance to the LPP-HPP interface motion due to precipitates is investigated. A circular precipitate region with the radius of R is located at the center of a square sample with the size L. The lower left corner is fixed in both x and y directions and the upper left corner is fixed only in the x direction. Initially, to avoid nucleation problem, a small part of the left side of the sample is considered a HPP and the rest of it is considered a LPP. Nucleation at a precipitate or inclusion was studied in [11] using the same PFA and is not relevant for the current problem on the determination of the interface friction. At low temperatures, the initial sharp interface between the HPP and LPP broadens to a diffuse interface which propagates to the right (direct PT), while at high temperatures a reverse PT occurs, and the interface moves back to the left. In the absence of the precipitate, slightly below the phase equilibrium temperature θ_{ℓ} , the interface propagates to the right and slightly above θ_{ℓ} it moves back to the left. Thus, there is no athermal resistance for direct and reverse PTs and there exists no athermal hysteresis. Due to the presence of a precipitate, the motion of an LPP-HHP interface experiences athermal resistance. Thus, a larger dimensionless thermal driving force $\bar{\theta} = (\theta_e - \theta)/\theta_e$ (or equivalent dimensionless mechanical driving force $\bar{p} = (p - p_e)/p_e$ for the loading with pressure) is required for the interface motion to continue to the right during the direct PT. Conversely, a smaller negative thermal driving force is required to allow the interface pass through the precipitate to the left during the reverse PT. Investigating such hysteresis is the main focus of the current study.

The critical thermal driving force for the direct PT, $\bar{\theta}_c^d$ (blue lines), and reverse PTs, $\bar{\theta}_c^r$ (red lines), are plotted vs. the misfit strain coefficient in Fig. 1a for the misfit strain distribution using the error function and in Fig. 1b for the constant misfit strain. They are defined as the temperatures for which stationary solutions with two-phase regions cease to exist, and solution evolve to the complete HPP for direct PT or complete LPP for the reverse PT. Between $\bar{\theta}_c^d$ and $\bar{\theta}_c^r$, two-phase equilibrium is arrested, which exhibit itself as an athermal resistance to the interface motion. In these simulations, L=20 and R=0.5 (i.e., c = 0.002), which is much smaller than the interface width of $\delta_0 = 1.43$. An important finding here is that the misfit strain does not practically show any effect on the critical thermal driving forces for the direct and reverse PTs provided that the precipitate radius size is small compared to the interface width. The difference between the critical thermal driving forces of direct and reverse PTs, $H = \bar{\theta}_c^d - \bar{\theta}_c^r$, defines the athermal hysteresis. Since the counterpart of the phase equilibrium temperature for the system with precipitate cannot be

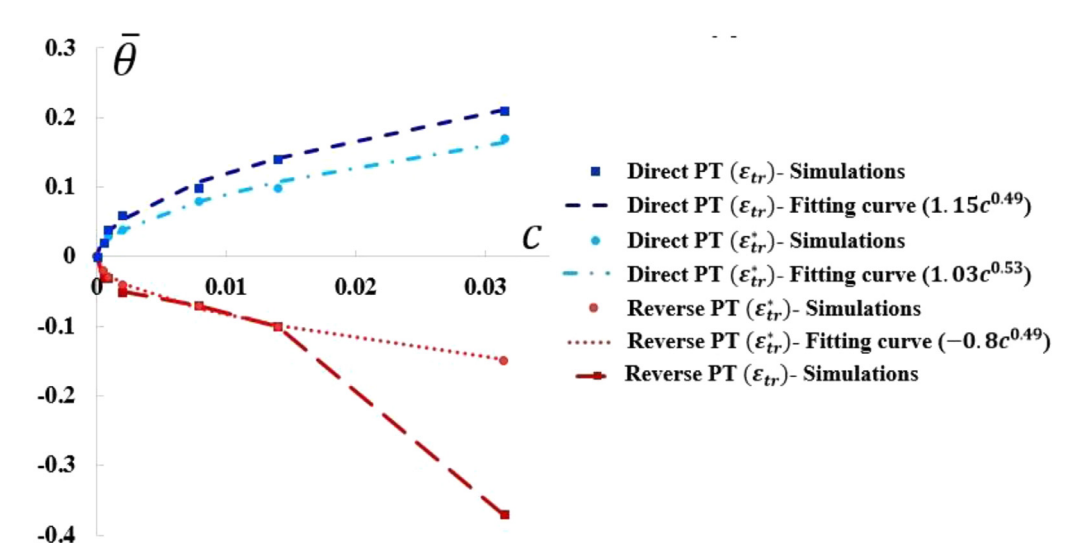


Fig. 2. The critical thermal driving forces vs. the precipitate concentration for the direct and reverse PTs for two different HPP transformation strain tensors, CSE BCs for R=2 and $\varepsilon_V=0.05$ combined with their fitting curves

determined, we assume that it is in the middle between $\bar{\theta}_c^d$ and $\bar{\theta}_c^r$, and the athermal resistance to the interface motion is the same in both direction and equal to 0.5H. For example, $\bar{\theta}_c^d = 0.04$ (or equivalently $\theta_c^d = 96K$), $\bar{\theta}_c^r$ (or equivalently $\theta_c^r = 106K$); thus, the athermal hysteresis is H = 0.10 (or equivalently |H| = 10K) for $\varepsilon_V = 0.02$ in Fig. 1b.

Note that even for misfit strain $\varepsilon_{\rm V}=0$, finite transformation strains in the matrix creates a remarkable misfit strain with the precipitate which causes a finite deformation in its shape and consequently, difference in the critical driving forces for direct and reverse PT. Such deformation is larger for larger precipitates, that is why the difference in the critical driving force for $\varepsilon_{\rm V}=0$ is larger for R=2 (Fig. 5) than for R=0.5 (Fig. 1).

By varying the sample size L in the range of 5–50 at constant R=2, the critical thermal driving forces and the hysteresis region are obtained vs. the precipitate concentration (Fig. 2). Obviously, point (0,0) is added for the sample without precipitate. The critical thermal driving forces nonlinearly increases like c^x , x = 0.49 - 0.53, vs. the precipitate concentration c for both the direct and reverse PTs, especially for low precipitate concentrations. The critical thermal driving forces for the direct and reverse PTs are approximately symmetric with respect to $\bar{\theta} = 0$ up to c = 0.015 and asymmetric above it. The asymmetry is due to the small sample as well as the compressive diagonal transformation strains of the HPP $\left(\epsilon_{tr} = \begin{bmatrix} -0.05 & 0.1 \\ 0.1 & 0.1 \end{bmatrix} \right)$ which produces

tion strains of the HPP $\begin{pmatrix} \boldsymbol{\varepsilon}_{tr} = \begin{bmatrix} -0.05 & 0.1 \\ 0.1 & -0.05 \end{bmatrix} \end{pmatrix}$ which produces tensile mean stress in the matrix and promotes reverse PT and suppresses the direct PT. Indeed, for zero diagonal transformation strains, i.e., $\boldsymbol{\varepsilon}_{tr}^* = \begin{bmatrix} 0 & 0.1 \\ 0.1 & 0 \end{bmatrix}$, the critical thermal driving forces $\bar{\theta}_c^d$

and $\bar{\theta}_c^r$ are almost symmetric with respect to $\bar{\theta}=0$. Note that plots in Fig. 2 are almost the same for any ε_V in the range $0 \le \varepsilon_V \le 0.1$, as expected from Fig. 1, while the critical thermal driving force depends on the misfit strain for larger precipitate sizes, which will be discussed later.

Now, let us consider a precipitate with R=2 and $\varepsilon_{\rm V}=0.05$. Fig. 3 presents the evolution of the HPP phase for the critical thermal driving force for the direct PT $\bar{\theta}_c^d=0.21$ (a), for a slightly larger thermal driving force $\bar{\theta}=0.22$ (b) and during the reverse PT for a slightly smaller thermal driving force $\bar{\theta}=-0.12$ than the critical thermal driving force $\bar{\theta}_c^r=-0.11$, when the CSE BCs are applied on the precipitate surface. For $\bar{\theta}_c^d=0.21$, the LPP-HPP interface propagates to the right until it reaches the precipitate and

stuck, and only slightly rotates at the upper side until it reaches the stationary solution at t=40 (Fig. 3a). Interface below the precipitate is delayed in comparison with the interface above the precipitate due to change in geometry caused by the transformation shear. After increasing the thermal driving force to $\bar{\theta}=0.22$, the interface passes through the precipitate region and completes the PT to the HPP in the entire sample at t=100 (Fig. 3b). The main event that determines unlimited interface motion is the loss of the stability of the stationary interface near the lower portion of the precipitate. This will be discussed later using the transformation work distribution. Due to the small sample size and the boundary effects, the interface significantly rotates around the precipitate before it leaves its surface. For larger sample sizes, the interface passes the precipitate region without changing its orientation.

For the reverse PT, to avoid nucleation problem like the one for the direct PT, we start simulations before complete direct PT occurs. Here, the solution of Fig. 3b at t=90 is chosen as the initial condition for the reverse PT problem as shown in Fig. 3c. Again, the main event that determines unlimited interface motion is the loss of the stability of the stationary interface near the lower portion of the precipitate, which is clearly delayed in Fig. 3c at t=110 and t=120 in comparison with that in the upper portion of the precipitate.

As it will be shown, variation in the precipitate surface energy changes the stress distribution and consequently transformation work and can significantly change the PT morphology and the critical thermal driving forces for both the direct and reverse PTs. Thus, the VSE is one of the key parameters in determining the critical thermal driving forces. Fig. 4 presents the evolution of the HPP phase (a) for direct PT for $\bar{\theta} = \bar{\theta_c^d} = 0.28$ up to the stationary solution and (b) for a slightly larger thermal driving force $\bar{\theta}=0.29$, as well as (c) during the reverse PT for a slightly smaller thermal driving force $\bar{\theta} = -0.02$ than the critical thermal driving force $\bar{\theta}_c^r = -0.01$ for the reverse PT, when the VSE BCs are applied on the precipitate surface. For VSE BCs, the surface energy of the boundary between the precipitate and the matrix varies from $1 J/m^3$ (for the LPP) to $0.6 J/m^3$ (for the HPP) in a very thin region with the width of 1 nm, while for CSE there is a practically sharp interface between precipitate and matrix for any phase. This significantly changes the stress distribution. For $\bar{\theta} = \bar{\theta}_c^d = 0.28$, after the LPP-HPP interface is arrested, its middle part coincides with the precipitate surface and its upper part rotates by 60° until it reaches the stationary solution at t = 200 (Fig. 4a).

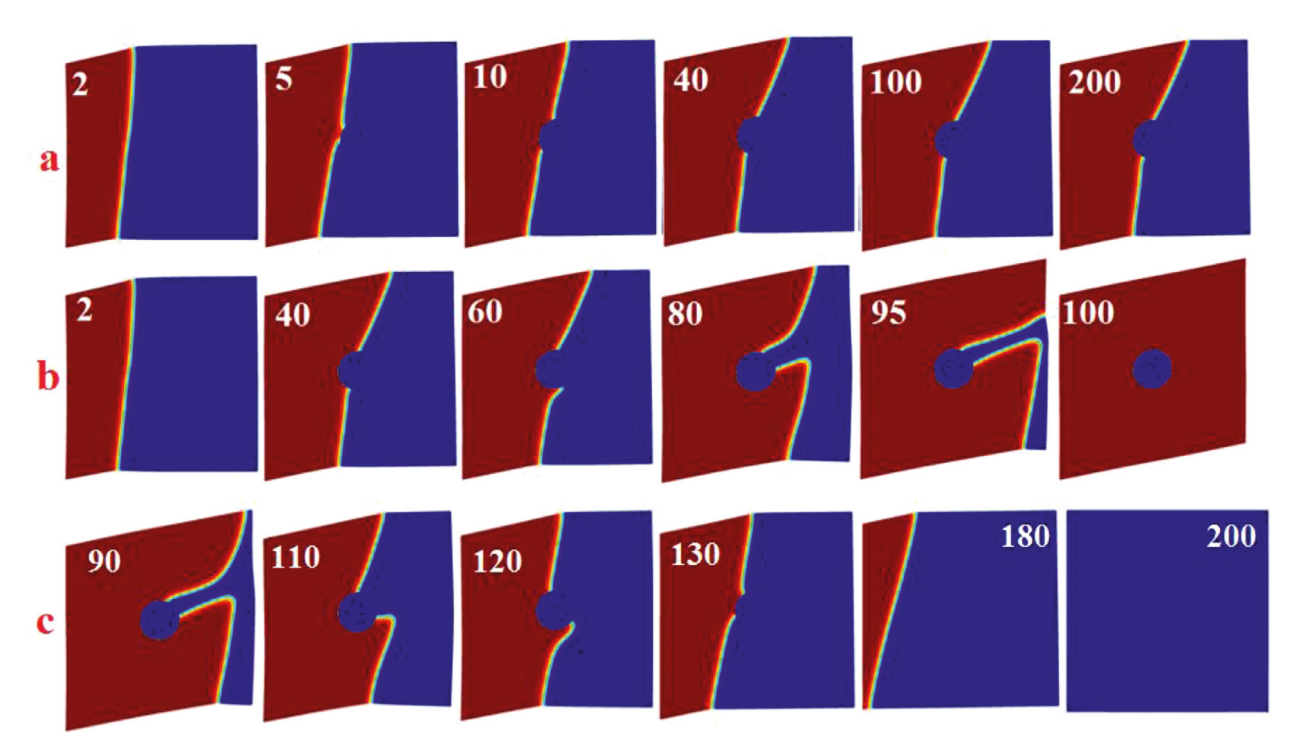


Fig. 3. The evolution of the HPP phase for the critical thermal driving force $\tilde{\theta}^d_c = 0.21$ up to stationary solution (a), for a slightly larger thermal driving force $\tilde{\theta} = 0.22$ (b), and for the thermal driving force $\tilde{\theta} = -0.12$ slightly smaller than the critical thermal driving force $\tilde{\theta}^r_c = -0.11$ for the reverse PT (c), all for CSE BCs at the precipitate surface. L= 20, R=2, and $\varepsilon_V = 0.05$.

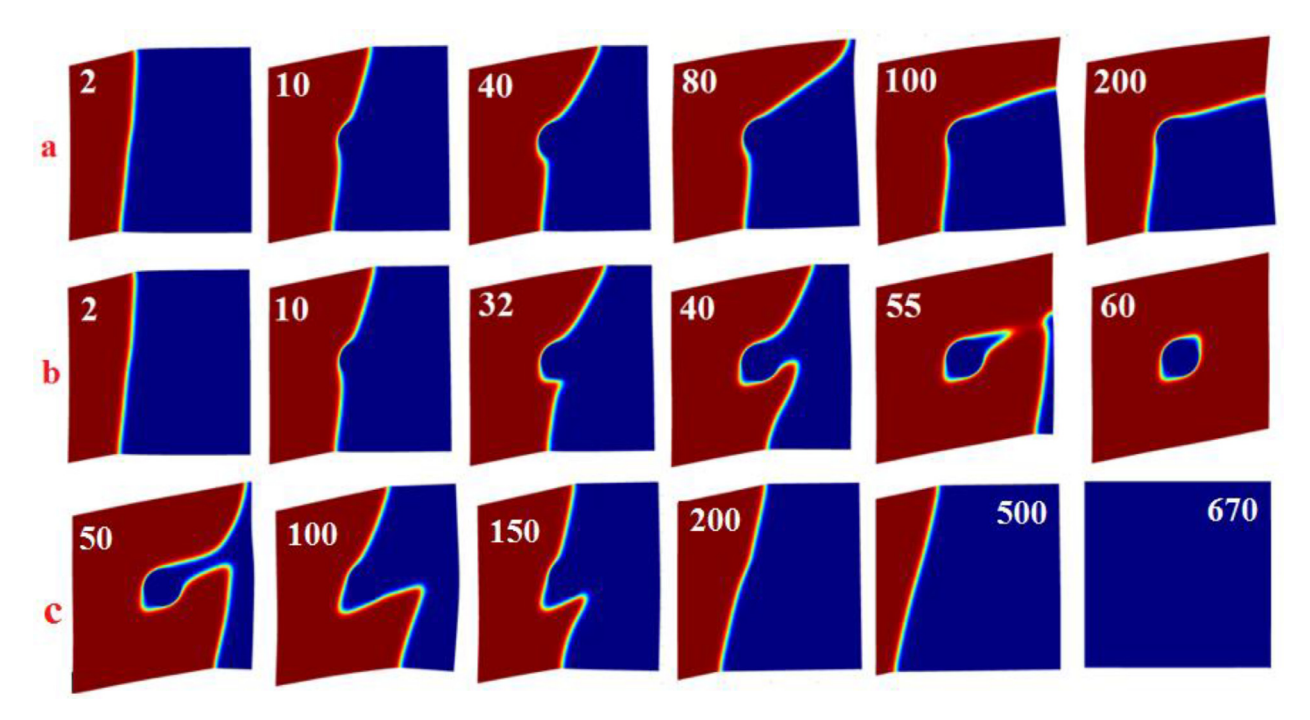


Fig. 4. The evolution of the HPP phase for the critical thermal driving force $\tilde{\theta} = \tilde{\theta}_c^d = 0.28$ up to stationary solution (a), for a slightly larger thermal driving force $\tilde{\theta} = 0.29$ (b), and for the thermal driving force $\tilde{\theta}_c = -0.01$ for the reverse PT (c) for VSE BCs at the precipitate surface. L= 20, R=2, and $\varepsilon_v = 0.05$.

Slightly increasing the thermal driving force to $\bar{\theta}=0.29$ results in a very different morphology so that the upper and lower parts of the interface continue propagation until they coalesce and move away from the precipitate (Fig. 4b). Similar to the discussion for Fig. 3, a non-complete transformed solution at t=50 from Fig. 4b is chosen as the initial condition for the reverse PT (Fig. 4c). In contrast to the CSE BCs, the reverse PT reveals a different evolution

compared to the direct PT, especially when passing the precipitate region (Fig. 4c).

The critical thermal driving forces vs. the misfit strain coefficient are plotted for both the direct and reverse PTs for R=2 (i.e., for the precipitate size larger than the interface width) in Fig. 5. For both the CSE and VSE BCs, the critical thermal driving force linearly increases vs. the misfit strain coefficient for the direct PT

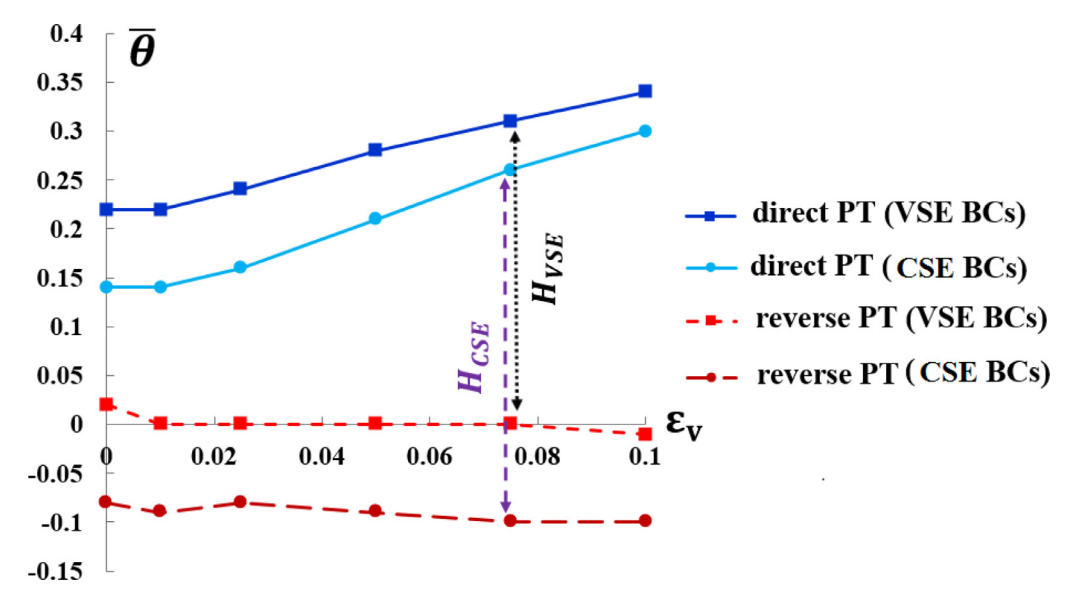


Fig. 5. The critical thermal driving forces vs. the misfit strain coefficient for the direct and reverse PTs for the CSE BCs and VSE BCs at the precipitate surface for R=2 nm and L=20. The hysteresis range is also shown.

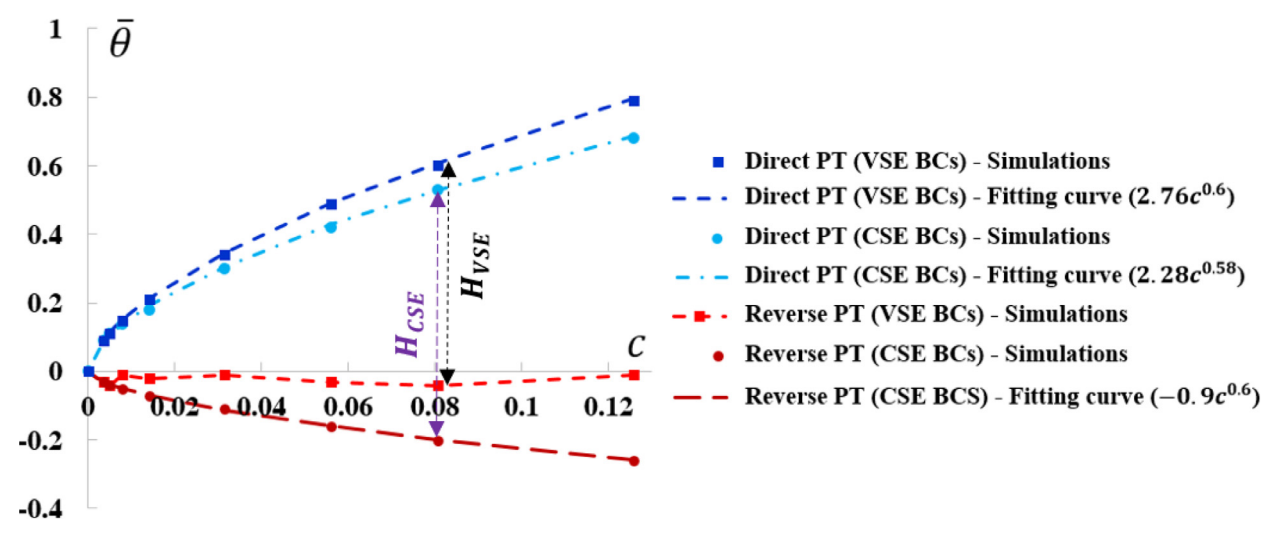


Fig. 6. The critical thermal driving forces for both the direct and reverse PTs and for both the VSE and CSE BCs vs. the precipitate concentration for $\varepsilon_v = 0.1$. R=2, 10 < L < 100, combined with their fitting curves

while it is almost independent of the misfit strain coefficient for the reverse PT. The VSE BCs also result in higher critical thermal driving forces for both the direct and reverse PTs and a smaller hysteresis compared to those of the CSE BCs. For example, for $\varepsilon_{v}=0.08$, $\bar{\theta}_{c}^{d}=0.31$ and $\bar{\theta}_{c}^{r}=0$ for the VSE which gives the hysteresis $H_{VSE}=0.31$ while for the CSE BCs, $\bar{\theta}_{c}^{d}=0.26$ and $\bar{\theta}_{c}^{r}=-0.1$ with the $H_{CSE}=0.36$. In comparison with Fig. 1, increase in R increases athermal hysteresis and suppress direct PT more than the reverse PT, due to stronger effect of volumetric transformation strain combined with misfit strain.

The critical thermal driving force for both the direct and reverse PTs and for both the VSE and CSE BCs are plotted vs. the precipitate concentration in Fig. 6 for $\varepsilon_{\rm V}=0.1$. In contrast to the problem with the small precipitate radius of R=0.5, the critical thermal driving force nonlinearly increases like $c^{\rm x}$, x=0.58-0.6, vs. the precipitate concentration for the direct PT. For the reverse PT, the critical thermal driving force for the CSE BCs also nonlinearly increases like $c^{\rm x}$, x=0.6, vs. the precipitate concentration c while it is almost independent of the precipitate concentration for the VSE BCs. Also, for any concentration, the VSE BCs result in higher crit-

ical thermal driving forces for both the direct and reverse PTs and a smaller hysteresis range compared to those of the CSE BCs.

From the computational point of view there are two choices to change the precipitate concentration: one is to keep the sample size while varying the precipitate radius and the other is to keep the precipitate radius constant and varying the sample size. The critical thermal driving forces for the two choices, i.e., (a) L=50 with varying precipitate radius from 1 to 6 and (b) R=2 with varying sample size from 15 to 100, are compared in Fig. 7 for $\varepsilon_{\rm v}=0.1$ and the CSE BCs. As can be seen in Fig. 7, even if we keep the sample size constant and change the precipitate size without changing the temperature, interface energy, and/or formation energy of phases, the results are very similar to the second case especially smaller concentrations of $c \le 1\%$. On the other hand, the precipitate/particle concentration in previous studies is very low. For example, the atomic fractions of particles in alloys [1,28] is mostly below 0.01%, the particle volume fraction of 0.05% is reported in [18], the volume fraction for nanoparticles is below 0.4% in [22] and much below 0.01% in [23] and so on. Thus, our results are practically valid for the precipitate/particle concentration

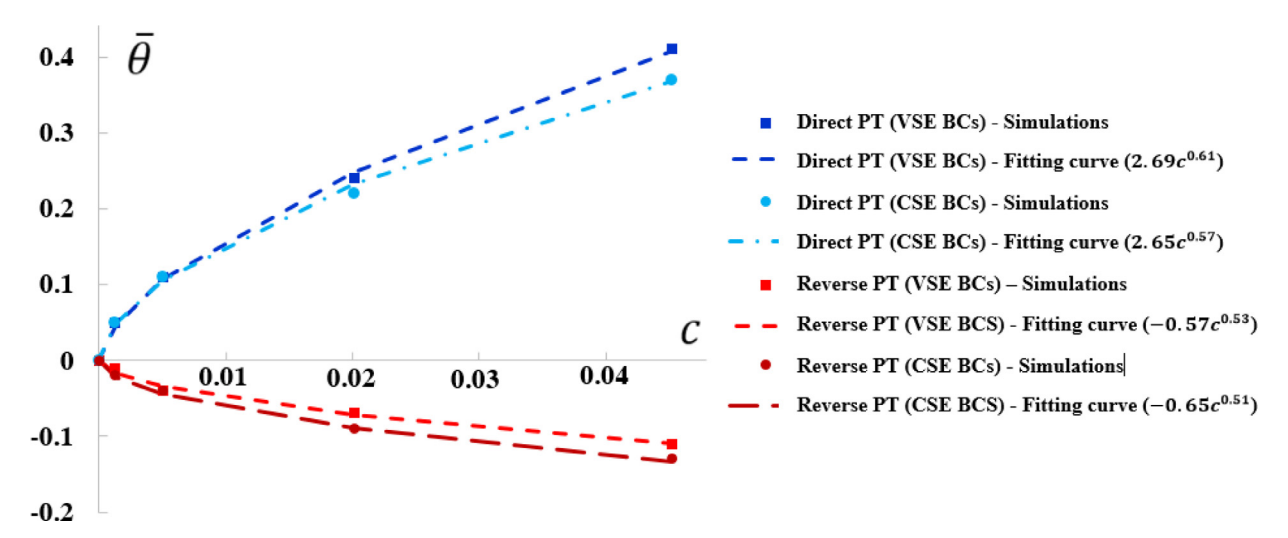


Fig. 7. The critical thermal driving forces for the direct and reverse PTs for two choices, i.e., (a) L=50 with varying precipitate radius and (b) R=2 with varying sample size, for $\varepsilon_v = 0.1$ and the CSE BCs, combined with their fitting curves

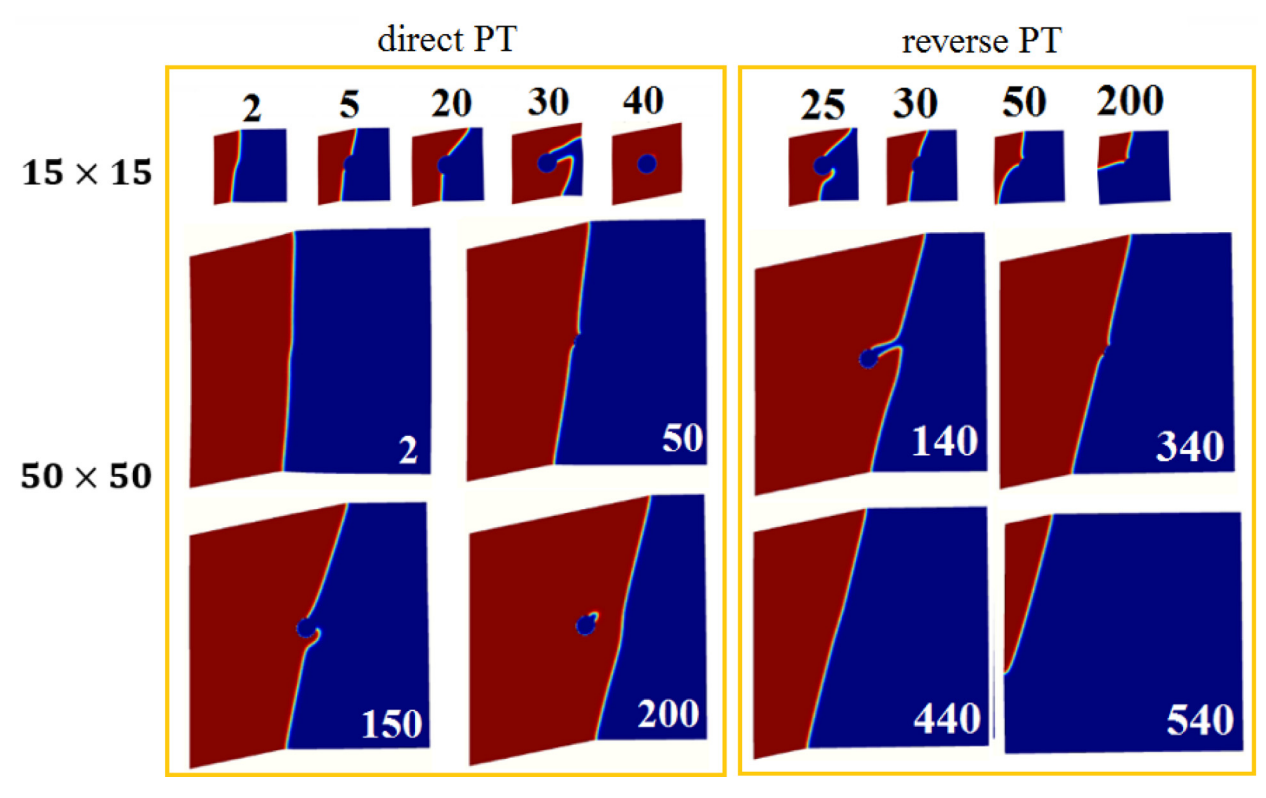


Fig. 8. The evolution of the HPP for the direct and reverse PTs for two different sample sizes of L=15 and 50 (R = 2). For the direct PT, $\tilde{\theta}=0.42$ for L=15 and $\tilde{\theta}=0.12$ for L=50 (slightly larger than their critical thermal driving forces). For the reverse PT, $\tilde{\theta}=-0.16$ for L = 15 and $\tilde{\theta}=-0.05$ for L = 50 (slightly smaller than their critical thermal driving forces).

discussed in previous studies. Even for the larger concentrations, the two methods differ only by maximum10–15% which is still an acceptable difference. This difference means that the effect of the third scale parameter, the phase interface width, can be significant only for very highly dense precipitate distribution.

Besides the variation of the critical athermal driving forces for the direct and reverse PTs with the concentration of the precipitate c (Fig. 6), the morphology and the transformation rate also show a remarkable dependence on c. The dependence of the evolution of the HPP on c is shown in Fig. 8 for the direct and reverse PTs for two different sample sizes of L=15 and 50 ($\varepsilon_{\rm V}=0.1$, R=2). Also,

the phase concentration $\bar{\eta}$ vs. time is plotted for different sample sizes L=10, 12.5, 15, 20, 30, 40 and 50 for the direct PT in Fig. 9. For smaller sizes, i.e., larger precipitate concentrations, the effect of the precipitate is much larger so that the transformation rate during the interaction of precipitate and the interface is smaller (intermediate region). For larger sizes, this effect reduces so that such region disappears for L>30 and the concentration shows a linear variation, i.e., the transformation rate becomes the same before, during and after the interface passes the precipitate region. Obviously, for larger samples, the stationary solution is reached for larger times.

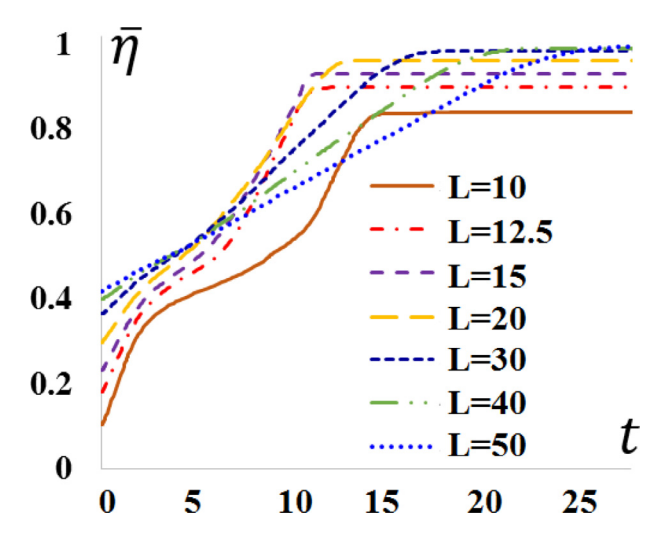


Fig. 9. The variation of the phase concentration $\bar{\eta}$ vs. for different sample sizes for the direct PT.

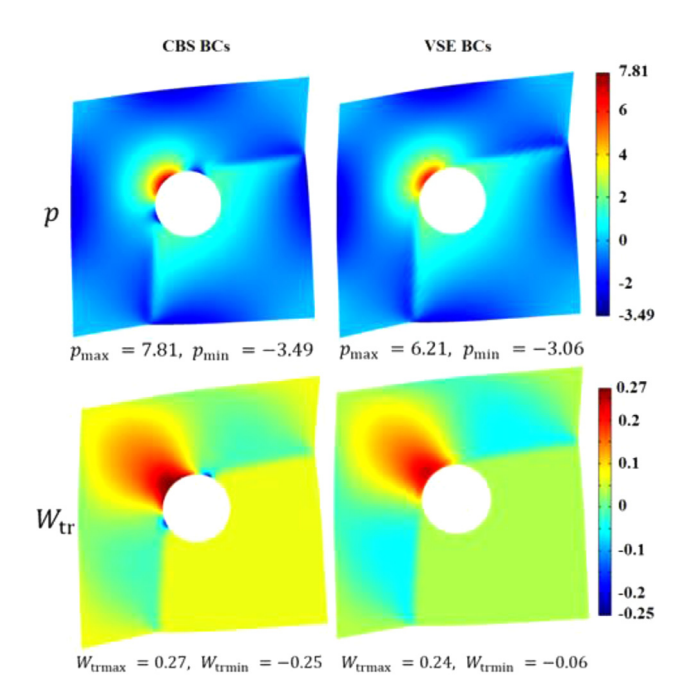


Fig. 10. The pressure distribution corresponding to the critical thermal driving force $\bar{\theta}_r^d=0.42$ for direct PT for the CSE and VSE BCs for c=0.056 and $\varepsilon_{\rm V}=0.1$.

The pressure and transformation work $(W_{tr} = \sigma : \varepsilon_{tr}(\eta) - z(\theta - \theta_e))$ distributions corresponding to the critical thermal driving force $\bar{\theta}_c^d = 0.42$ for direct PT are plotted in Fig. 10 for both the CSE and VSE BCs for c = 0.056 and $\varepsilon_{\rm V} = 0.1$. For a better illustration of the pressure inside the transforming region, the precipitate is excluded. Due to the VSE BCs, the precipitate is surrounded by the LPP and a continuous interface, and it is under pressure. For the CSE BCs, a part of the precipitate surface is surrounded by the HPP with a larger pressure concentration than for the VSE BCs; tensile stresses appear at the intersection of the interface and the precipitate and the boundary region between the precipitate surface and the LPP is under pressure.

The transformation work also shows higher concentrations around the precipitate region in the HPP for the CSE BCs (\approx 0.25) than for the VSE BCs (\approx 0.2) but almost the same low values along the interface away from the precipitate. The difference between the transformation work values for the two BCs is not significant; thus,

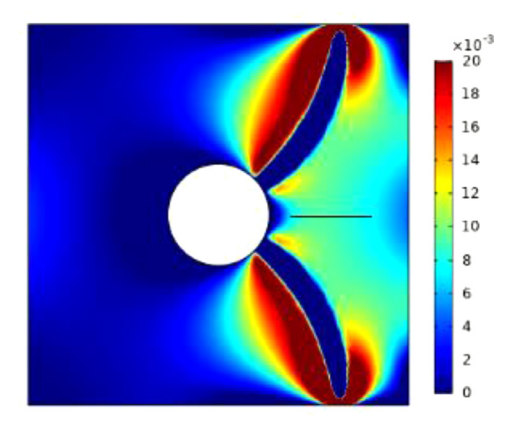


Fig. 11. The pressure distribution at $\bar{\theta} = \bar{\theta}_c^d = 0.06$ for R = 2nm, c = 0.053, without misfit and transformation strain, and with the CSE BCs. The pinning pressure (along the horizontal line shown in the figure) is in the range 0.008 - 0.01 *GPa*, which is in good agreement with the Zener theory.

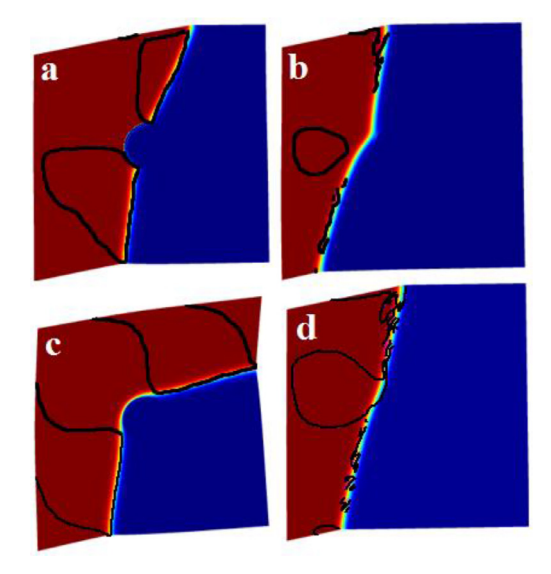


Fig. 12. The morphology of the HPP nanostructure at the critical thermal driving force for (a) the direct PT with the CSE BCs ($\tilde{\theta}_c^d = 0.21$), (b) the reverse PT with the CSE BCs ($\tilde{\theta}_c^d = -0.11$), (c) the direct PT with the VSE BCs ($\tilde{\theta}_c^d = 0.28$), and (d) the reverse PT with the VSE BCs ($\tilde{\theta}_c^r = -0.01$), combined with the contour line $W_e = 0$.

a low difference is expected between the critical thermal driving forces for the CSE and VSE BCs ($\bar{\theta}_c^d=0.42$ for the CSE BCs while $\bar{\theta}_c^d=0.49$ for the VSE BCs).

The main differences between the present study for the phase interface and the Zener theory for the grain boundary [46-49] are that our theory includes transformation strain due to PT, misfit strain in the precipitate, and variation in the surface energy during the PT. An important point is that if we neglect the transformation and misfit strains and variable surface energy, and only consider the interface stresses due to the surface energy between the precipitate and the matrix (introduced in [34] and used in many papers such as [35,50]), we obtain good correspondence with the Zener theory. From the Zener theory [46–49], for the plane strain problem with cylindrical precipitates, the pinning pressure $p_{pin} = \frac{4c\gamma \sin\alpha}{\pi R}$, where α is the angle between the normal to the interface motion before reaching the precipitate and the interface tangent at the intersection of the interface and the precipitate surface. The pinning pressure is in fact the pressure exerted by particles to prevent the motion of an interface, which counteracts the interface driving force and depends on the interface energy and the volume fraction and size of particles. For parameters like in our

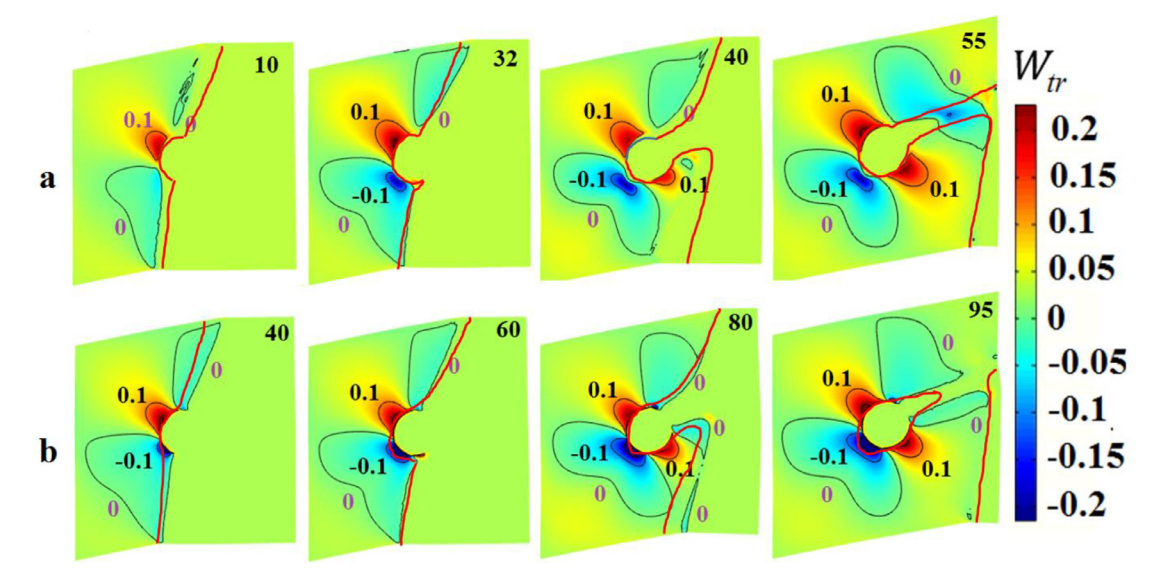


Fig. 13. The evolution of the transformation work W_{tr} during the direct PT for the CSE BCs at $\tilde{\theta}=0.22$ (a) and for the VSE BCs at $\tilde{\theta}=0.29$ (b). The phase interfaces are included in each figure.

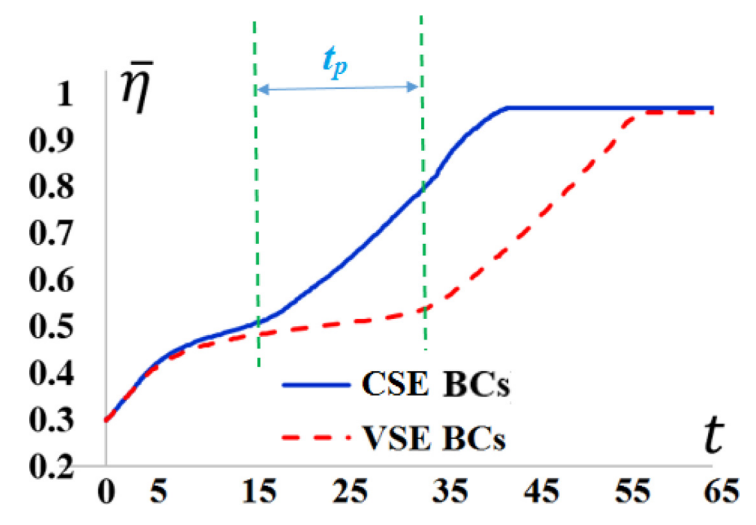


Fig. 14. The phase concentration $\bar{\eta}$ vs. time for the CSE and VSE BCs $\bar{\theta}=0.3$.

simulation in Fig. 11, namely, R=2nm, c=0.053, $\alpha\approx45^{\circ}$, and the surface energy $\gamma=0.36$, we obtain $p_{pin}=0.0085$ *GPa*. The pressure distribution obtained from the simulations in Fig. 11 gives the pinning pressure (along the horizontal line shown in the figure) in the range 0.008-0.01 *GPa*, which is in good agreement with the Zener theory. When we do not neglect misfit and transformation strains, the pinning pressure along the horizontal line shown in Fig. 10 is on the order of GPa, i.e., much larger than the Zener pinning pressure. The athermal hysteresis for neglected misfit and transformation strains is also expectedly smaller. Thus, the critical thermal driving force for direct PT for neglected misfit and transformation strains is $\bar{\theta}_c^d=0.06$ while with the transformation misfit strains in Fig. 10 we have $\bar{\theta}_c^d=0.42$.

The obtained critical thermal driving forces are validated using the local phase equilibrium condition criterion. To do so, the contour of the equilibrium condition $W_e=\sigma:\epsilon_{tr}-z(\theta-\theta_e)=0$ [40] is plotted on the stationary HPP nanostructure at the critical thermal driving force for both the direct and reverse PTs and the VSE and CSE BCs in Fig. 12. It is seen that the interface well coincides with the phase equilibrium condition contour $W_e=0$, confirming thermodynamic phase equilibrium for the stationary solution.

To better show the highly heterogeneous stress field and the transformation work, the evolution of the transformation work $W_{tr} = \sigma : \varepsilon_{tr}(\eta) - z(\theta - \theta_e)$ during the direct PT is presented in Fig. 13 for the CSE BCs at $\bar{\theta}=0.22$ and for the VSE BCs at $\bar{\theta}=0.29$. The high tensile and compressive stress concentrations and consequently, transformation work concentrations appear near the precipitate. The suppression of the interface motion at the precipitate occurs in the regions of negative transformation work (blue regions). Also, the interface motion occurs the regions where $W_{tr} > 0$. Since for each type of BCs the evolution is obtained for a slightly larger thermal driving force than its critical value, the transformation work along the moving interface regions is relatively low and mainly $0 < W_{tr} < 0.05$. As stated earlier, the VSE BCs result in the higher critical thermal driving force than the CSE BCs and consequently, the PT is promoted by the CSE BCs. This can be seen from the variation of the phase concentration with time for $\bar{\theta} = 0.3$ as an example. The phase concentration $\bar{\eta}$ is defined as the ratio of the transformed area to the total area. As can be seen in Fig. 14, the phase concentration for the CSE BCs is larger than that for the VSE BCs. The main difference between the two solutions appears during the time period t_p when the interface is interacting with the precipitate and as it is clear, the rate of transformation is much

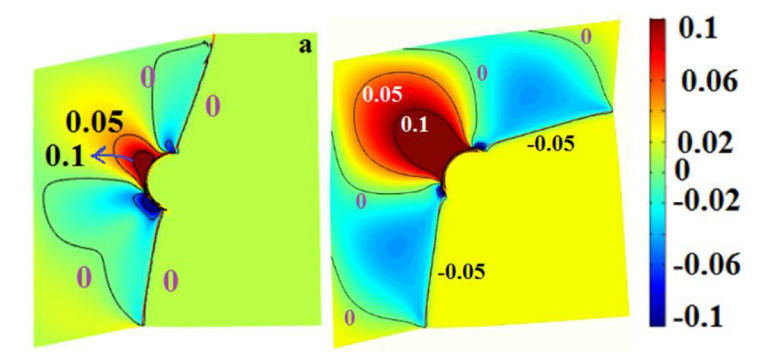


Fig. 15. The distribution of W_{tr} combined with the stationary interface contour lines of $\eta=0.5$ (red line) for $\varepsilon_{\rm v}=0.01$ at $\bar{\theta}_c^d=0.14$ (a) and $\varepsilon_{\rm v}=0.1$ at $\bar{\theta}_c^d=0.29$ (b) for the CSE BCs.

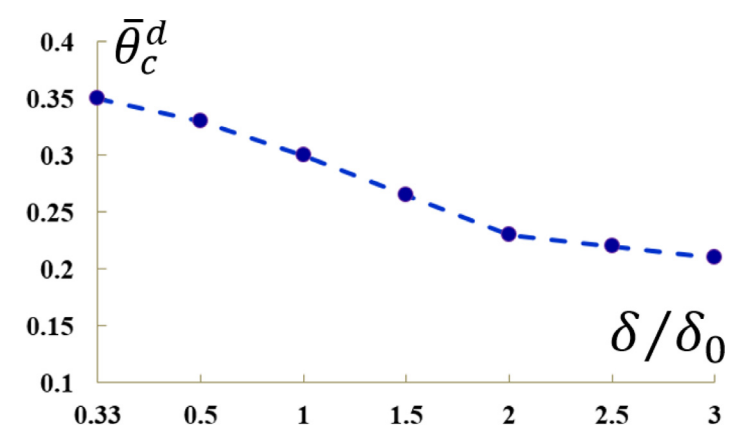


Fig. 16. The variation of the critical thermal driving force for direct PT vs. the normalized LPP-HPP interface width for the CSE at the precipitate surface and for c = 0.056 and $\varepsilon_v = 0.1$.

larger for the CSE BCs. After this period, the transformation rate is again similar for both cases until they reach their stationary solutions. As a result, the stationary solution for the CSE BCs is reached at a shorter time (t = 38) than for the VSE BCs (t = 55).

It is worthy to note that the significant rotation of the stationary interface not only can be caused by the VSE BCs (like in Fig. 12), but also occurs for the large misfit strains even for the CSE BCs. Fig. 15 shows the distribution of W_{tr} combined with the stationary interface contour lines of $\eta=0.5$ for two different misfit strain coefficients $\varepsilon_{\rm V}=0.01$ and 0.1, for the direct PT for the CSE BCs, and a significant rotation of the interface is found for the large misfit strain $\varepsilon_{\rm V}=0.1$. The interface contour also corresponds to the regions of $W_{tr}=0$ which proves its phase equilibrium state.

It is worthy to investigate the effect of interface width on the critical thermal driving force. In fact, by changing the interface width, the interaction of interface with precipitate surface changes which affects the critical thermal driving force. Here, the interface width is varied by changing parameter β and the critical thermal driving force is plotted vs. the normalized LPP-HPP interface width δ/δ_0 in Fig. 16 for direct PT for the CSE BCs at the precipitate surface and for c=0.056 and $\varepsilon_{\rm V}=0.1$. As can be seen, the critical thermal driving force almost linearly reduces from 0.35 to 0.21 within the interface width range from $\delta/\delta_0=0.33$ (closer to the sharp interface approach) to 3. A similar dependence of the results on the interface energy is also found for other used misfit strains and precipitate concentrations.

5. Concluding remarks

There are various types of correspondences of our results and previous theoretical and experimental results:

- Suppressive effect on the martensite start temperature and transformation rate due to precipitates that we obtained with PFA is documented in many experiments and MD simulations, e.g., [8,51–54].
- After neglecting all sophistications related to phase interface versus grain boundary, our results reporduce well the Zener theory for the grain boundary, which has numeorus confirmation by experiments, MD, and PFA. That means that at least concentration deprendence of the athermal interface friction and the effect of particle size and constant surface energy are catched correctly. We obtined that athermal friction in Zener theory is an order of magnitude smaller than when we include misfit and transformation strains.
- For phase interface, the effect of surface tension is much smaller than the misfit and transformation strain. Our precipitate/inclusion represents formally a center of dilatation, but with surface energy. However, solute atoms are modeled as centers of dilation a well, without surface energy. Thus, formally, we should have similar concentration dependence of the athermal friction due to solute atoms and precipitates. It is experimentally found that the athermal interface friction due to solute atoms for martensitic growth vs. the concentration of 14 alloying components such as Al, C, Co, Ni, ..., etc., in Febased alloys has a $c^{0.5}$ -dependence [1]. The fitting functions for our results for the direct and reverse PTs also show a similar c^{x} dependence of the athermal friction. For example, x = 0.53for the direct PT and x = 0.49 for the reverse PT (Fig. 2 for the CSE BCs), x = 0.6 for the direct PT (Fig. 6, CSE BCs), x = 0.58 for the direct PT and x = 0.6 for the reverse PT (Fig. 6, VSE BCs), x = 0.61 for the direct PT and x = 0.53 for the reverse PT (Fig. 6, VSE BCs), x = 0.58 for the direct PT and x = 0.6 for the reverse

PT (Fig. 7, VSE BCs), and x = 0.57 for the direct PT and x = 0.51 for the reverse PT (Fig. 7, CSE BCs).

- MD simulations revealed that larger precipitates and smaller spacings between precipitates (i.e., large concentration *c*) hinder the PT by impeding relaxation of internal elastic strains [52]. This is similar to our results where the larger the precipitate concentration, the larger the athermal interface friction. The ranges used for the precipitate size and spacing (below 12 nm) in [52] are also used in our simulations.

The above correspondence to some extends validates our approach.

The advantage of the PFA in comparison with atomistic simulations (in addition to possibility of consideration of larger time and space scales) is that allows to easily and independently change the material and geometric parameters and consider some generic models. In particular, inclusion can have arbitrary shape, size, surface energy, and other properties, while in atomistic simulations they are interrelated through chosen interatomic potential and energy minimization procedure. Suggested advanced PFA for determination of the athermal resistance to the LPP-HPP interface motion due to the precipitate/inclusion and corresponding nanostructure evolution allowed us to find the first main effects of the varied parameters for the generic model. We studied the effect of the misfit strain profile, transformation strain, variable during the PT surface energy, size and concentration of the inclusions, and phase interface width. The reasons for athermal friction and temperature/pressure PT hysteresis are the internal stress fields at the phase interface due to interface stresses, misfit and transformation strains, as well as change in the precipitate surface energy during PT. With increasing thermodynamic stimulus, by changing temperature or applied stresses/pressure, phase interface reaches critical unstable thermodynamically equilibrium configuration. After further increase in the stimulus, interface loses its stability complete PT occurs in a non-equilibrium way, dissipating energy. The same occurs for the reverse PT. Reduction in the precipitate surface energy by 40% during PT significantly changes the PT morphology and the athermal friction, so this is important parameter and should studied in more detail in future. For any concentration, the allowing for reduction in surface energy unexpectedly results in higher athermal friction, but expectedly in a smaller hysteresis and a larger transformation rate. The interface does not split when passing the precipitate for this case, but its width reduces.

Increase in the interface width reduces the interphase friction. We are not aware that these two parameters were included in explanation of the interface friction. Simultaneous effect of the precipitate radius normalized by the interface width and misfit strain is also nontrivial. For small radii, the misfit strain does not practically affect the interface friction. In the opposite case, for both the constant and variable precipitate surface energy, the athermal friction linearly increases vs. the misfit strain for the direct PT while it is almost independent of it for the reverse PT. Observed asymmetry in the athermal friction for the direct and reverse PT shows that traditional assumption that the phase equilibrium temperature/pressure is the averaged of those for direct and reverse PTs is not true. This asymmetry is, in particular, caused by transformation shear strain and different interface evolution, especially when passing the precipitate region. For the reverse PT, the interface friction for the CSE BCs linearly increases with the precipitate concentration, while it is almost independent of the precipitate concentration for the VSE BCs. For the same temperature, the CSE BCs create a larger thermal driving force compared to the VSE BCs, which results in a larger transformation rate during the interaction of the interface and the precipitate. The results of the two choices to change the precipitate concentration, i.e., the constant sample size with variable precipitate radius and the constant precipitate radius with variable sample size, coincide for smaller concentrations and slightly differ for larger concentrations. We demonstrated that the local thermodynamic driving force at the interface in the critical stationary configuration is zero, like in the sharp-interface theory. The suppression of the interface motion at the precipitate is found at the regions of negative transformation work, while the interface motion occurs in the regions with the positive transformation work. The morphology and the transformation rate also show a remarkable dependence on the concentration so that for smaller sizes, the effect of the precipitate is much larger and the transformation rate during the interaction is smaller. The obtained results give an important generic understanding of athermal friction mechanism for phase interfaces for various PTs at the nanoscale and show directions of the more detailed and focused studies.

Declaration of Competing Interest

The authors declare that they have no known competing financial interests or personal relationships that could have appeared to influence the work reported in this paper.

Acknowledgments

The support of Isfahan University of Technology and Iran National Science Foundation is for MJ gratefully acknowledged. VIL work was funded by NSF (MMN-1904830 and CMMI-1943710) and the ISU (Vance Coffman Faculty Chair Professorship), as well as XSEDE, allocation TG-MSS170015.

References

- G. Ghosh, G.B. Olson, Kinetics of FCC-BCC heterogeneous martensitic nucleation –I. The critical driving force for athermal nucleation, Acta Mater. 42 (10) (1994) 3361–3370.
- [2] M. Grujicic, G.B. Olson, W.S. Owen, Mobility of martensitic interfaces, Metall. Mater. Trans. A 16 (1985) 1713–1722.
- [3] V.I. Levitas, A.V. Idesman, G.B. Olson, E. Stein, Numerical modelling of martensitic growth in an elastoplastic material, Philos. Mag. A 82 (2002) 429–462.
- [4] A. Cuniberti, S. Montecinos, F.C. Lovey, Effect of γ2-phase precipitates on the martensitic transformation of a β-CuAlBe shape memory alloy, Intermetallics 17 (2009) 435-440.
- [5] J.I. Pérez-Landazábal, V. Recarte, D.S. Agosta, V. Sánchez-Alarcos, and R.G. Leisure. Defect pinning of interface motion in thermoelastic structural transitions of Cu-Al-Ni shape-memory alloy. Phys. Rev. B 73, 224101.
- [6] C.L. Gong, F.S. Han, Z. Li, M.P. Wang, Internal friction peak associated with the interface motion in the martensitic transformation of CuAlNiMnTi shape memory alloy, J. Appl. Phys. 102 (2007) 023521.
- [7] S. Ataollahi, M.J. Mahtabi, A molecular dynamics study on the effect of precipitate on the phase transformation in NiTi, in: Proceedings of the Research Dialogues Conference, 2021.
- [8] S. Ataollahi, M.J. Mahtabi, Effects of precipitate on the phase transformation of single-crystal NiTi alloy under thermal and mechanical loads: a molecular dynamics study, Mater. Today Commun. 29 (2021) 102859.
- [9] C. Chluba, et al., Ultralow-fatigue shape memory alloy films, Science 348 (6238) (2015) 1004–1007.
- [10] H. Hou, et al., Fatigue-resistant high-performance elastocaloric materials via additive manufacturing, Science 366 (6469) (2019) 1116–1121.
- [11] A. Basak, V.I. Levitas, Matrix-precipitate interface-induced martensitic transformation within nanoscale phase field approach: Effect of energy and dimensionless interface width, Acta Mater. 189 (2020) 255–265.
- [12] V.I. Levitas, D.W. Lee, Athermal resistance to interface motion in the phase-field theory of microstructure evolution, Phys. Rev. Lett. 99 (2006) 245701.
- [13] V.I. Levitas, D.W. Lee, D.L. Preston, Interface propagation and microstructure evolution in phase field models of stress-induced martensitic phase transformations, Int. J. Plast. 26 (2010) 395–422.
- [14] V.I. Levitas, M. Javanbakht, Phase field approach to interaction of phase transformation and dislocation evolution, Appl. Phys. Lett. 102 (2013) 251904.
- [15] V.I. Levitas, High pressure phase transformations revisited, J. Phys. Condens. Matter 30 (2018) 163001.
- [16] V.I. Levitas, High-pressure phase transformations under severe plastic deformation by torsion in rotational anvils, Mater. Trans. 60 (7) (2019) 1294–1301.
- [17] V.I. Levitas, Phase transformations, fracture, and other structural changes in inelastic materials, Int. J. Plast. 140 (102914) (2021) 1–51.
- [18] G. Couturier, et al., Finite element simulations of 3D Zener pinning, Mater. Sci. Forum 467–470 (Oct. 2004) 1009–1018 Trans Tech Publications, Ltd..

[19] N. Fujiyama, et al., Austenite grain growth simulation considering the solutedrag effect and pinning effect, Sci. Technol. Adv. Mater. 18 (1) (2017) 88–95.

- [20] Z. Li, J. Wang, H. Huang, Influences of grain/particle interfacial energies on second-phase particle pinning grain coarsening of polycrystalline, J. Alloy. Compd. 818 (2020) 152848.
- [21] R.K. Koju, K.A. Darling, K.N. Solanki, Y. Mishin, Atomistic modeling of capillarydriven grain boundary motion in Cu-Ta alloys, Acta Mater. 148 (2018) 311–319.
- [22] D. Chen, T. Ghoneim, Y. Kulkarni, Effect of pinning particles on grain boundary motion from interface random walk, Appl. Phys. Lett. 111 (2017) 161606.
- [23] A.R. Eivani, et al., Effect of the size distribution of nanoscale dispersed particles on the zener drag pressure, Metall. Mater. Trans. A 42 (2011) 1109–1116.
- [24] Y. Li, J. Zhou, R. Li, Q. Zhang, Molecular dynamics simulation of zener pinning by differently shaped and oriented particles, Front. Mater. 8 (2021) 682422.
- [25] H.L. Yang, et al., Study on recrystallization and correlated mechanical properties in Mo-modified Zr-Nb alloys, Mater. Sci. Eng. A 661 (2016) 9–18.
- [26] A. Graux, et al., Precipitation and grain growth modelling in Ti-Nb microalloyed steels, Materialia 5 (2019) 100233.
- [27] A.V. Mikhaylovskaya, M.E. Ghayoumabadi, A.G. Mochugovskiy, Superplasticity and mechanical properties of Al-Mg-Si alloy doped with eutectic-forming Ni and Fe, and dispersoid-forming Sc and Zr elements, Mater. Sci. Eng. A 817 (2021).
- [28] H. Dong, et al., Analysis of the interaction between moving α/γ interfaces and interphase precipitated carbides during cyclic phase transformations in a Nb-containing Fe-C-Mn alloy, Acta Mater. 158 (2018) 167–179.
- [29] C. Schwarze, R.D. Kamachali, I. Steinbach, Phase-field study of zener drag and pinning of cylindrical particles in polycrystalline materials, Acta Mater. 106 (2016) 59–65.
- [30] K. Chang, J. Kwon, C.K. Rhee, Effect of particle-matrix coherency on Zener pinning: a phase-field approach, Comput. Mater. Sci. 142 (2018) 297–302.
- [31] T. Chakrabarti, S. Manna, Zener pinning through coherent precipitate: a phase-field study, Comput. Mater. Sci. 154 (2018) 84–90.
- [32] N. Moelans, B. Blanpain, P. Wollants, Phase field simulations of grain growth in two-dimensional systems containing finely dispersed second-phase particles, Acta Mater. 54 (4) (2006) 1175–1184.
- [33] V.I. Levitas, D.L. Preston, Three-dimensional Landau theory for multivariant stress induced martensitic phase transformations. I. Austenite-martensite, Phys. Rev. B 66 (2002) 134206.
- [34] V.I. Levitas, D.L. Preston, Three-dimensional Landau theory for multivariant stress induced martensitic phase transformations. II. Multivariant phase transformations and stress space analysis, Phys. Rev. B 66 (2002) 134207.
- [35] V.I. Levitas, D.L. Preston, D.W. Lee, Three-dimensional Landau theory for multivariant stress-induced martensitic phase transformations. III. Alternative potentials, critical nuclei, kink solutions, and dislocation theory, Phys. Rev. B 68 (2003) 134201.
- [36] V.I. Levitas, M. Javanbakht, Surface tension and energy in multivariant martensitic transformations: phase-field theory, simulations, and model of coherent interface, Phys. Rev. Lett. 105 (2010) 165701.

- [37] M. Javanbakht, E. Barati, Martensitic phase transformations in shape memory alloy: phase field modeling with surface tension effect, Comput. Mater. Sci. 115 (2016) 137–144.
- [38] S. Mirzakhani, M. Javanbakht, Phase field-elasticity analysis of austenite—martensite phase transformation at the nanoscale: Finite element modeling, Comput. Mater. Sci. 154 (2018) 41–52.
- [39] V.I. Levitas, M. Javanbakht, Phase-field approach to martensitic phase transformations: effect of martensite-martensite interface energy, Int. J. Mater. Res. 102 (2011) 652–665.
- [40] M. Javanbakht, V.I. Levitas, Nanoscale mechanisms for high-pressure mechanochemistry: a phase field study, J. Mater. Sci. 53 (2018) 13343–13363.
- [41] V.I. Levitas, M. Javanbakht, Phase transformations in nanograin materials under high pressure and plastic shear: nanoscale mechanisms, Nanoscale 6 (2014) 162–166.
- [42] M. Javanbakht, V.I. Levitas, Interaction between phase transformations and dislocations at the nanoscale. Part 2: phase field simulation examples, J. Mech. Phys. Solids 82 (2015) 164–185.
- [43] M. Javanbakht, V.I. Levitas, Phase field simulations of plastic strain-induced phase transformations under high pressure and large shear, Phys. Rev. B 94 (2016) 214104.
- [44] Y. Wang, L. Peng, Y. Wu, Y. Zhao, Y. Wang, Y. Huang, W. Ding, Phase-field modeling the effect of misfit on the precipitation of the second-phase particles and grain coarsening, Comput. Mater. Sci. 100 (2015) 166–172.
- [45] J. Kundin, H. Emmerich, J. Zimmer, Three-dimensional model of martensitic transformations with elasto-plastic effects, Philos. Mag. 90 (11) (2010) 1495–1510.
- [46] R.K. Koju, K.A. Darling, L.J. Kecskes, Y. Mishin, Zener Pinning of grain boundaries and structural stability of immiscible alloys, JOM 68 (6) (2016) 1596–1604.
- [47] E. Nes, N. Ryum, O. Hunderi, On the Zener drag, Acta Metall. 33 (1985) 11–22.
- [48] P.A. Manohar, M. Ferry, T. Chandra, Five decades of the Zener equation, ISIJ Int. 38 (1998) 913–924.
- [49] W.B. Li, K.E. Easterling, The influence of particle shape on Zener drag, Acta Metall. Mater. 38 (1990) 1045–1052.
- [50] D.J. Seol, S.Y. Hu, Y.L. Li, L.Q. Chen, K.H. Oh, Cubic to tetragonal martensitic transformation in a thin film elastically constrained by a substrate, Met. Mater. Int. 9 (2003) 221–226.
- [51] H. Luo, F. Shan, Y. Huo, Y. Wang, Effect of precipitates on phase transformation behavior of Ti-49 at.% Ni film, Thin Solid Films 339 (1-2) (1999) 305–308.
- [52] E. Zarkadoula, Y. Yang, A. Borisevich, E. George, Effects of precipitate size and spacing on deformation-induced fcc to bcc phase transformation, Mater. Res. Lett. 10 (9) (2022) 585–592.
- [53] J. Chen, D. Huo, H.K. Yeddu, Molecular dynamics study of phase transformations in NiTi shape memory alloy embedded with precipitates, Mater. Res. Exp. 8 (10) (2021) 106508.
- [54] H. Luo, F. Shan, Y. Huo, Y. Wang, Effect of precipitates on phase transformation behavior of Ti-49 at.% Ni film, Thin Solid Films 339 (1,2) (1999) 305–308.